nature nanotechnology

ARTICLES

https://doi.org/10.1038/s41565-021-00926-z

Check for updates

# Viscoelastic surface electrode arrays to interface with viscoelastic tissues

Christina M. Tringides[1,2,3], Nicolas Vachicouras[4], Irene de Lázaro[3,5], Hua Wang[3,5], Alix Trouillet[4], Bo Ri Seo[3,5], Alberto Elosegui-Artola[3,5,6], Florian Fallegger[4], Yuyoung Shin[7], Cinzia Casiraghi[7], Kostas Kostarelos[8,9], Stéphanie P. Lacour[4] and David J. Mooney[3,5]✉

**Living tissues are non-linearly elastic materials that exhibit viscoelasticity and plasticity. Man-made, implantable bioelectronic arrays mainly rely on rigid or elastic encapsulation materials and stiff films of ductile metals that can be manipulated with microscopic precision to offer reliable electrical properties. In this study, we have engineered a surface microelectrode array that replaces the traditional encapsulation and conductive components with viscoelastic materials. Our array overcomes previous limitations in matching the stiffness and relaxation behaviour of soft biological tissues by using hydrogels as the outer layers. We have introduced a hydrogel-based conductor made from an ionically conductive alginate matrix enhanced with carbon nanomaterials, which provide electrical percolation even at low loading fractions. Our combination of conducting and insulating viscoelastic materials, with top-down manufacturing, allows for the fabrication of electrode arrays compatible with standard electrophysiology platforms. Our arrays intimately conform to the convoluted surface of the heart or brain cortex and offer promising bioengineering applications for recording and stimulation.**

Implantable electrode arrays interface with tissues such as the brain and heart[1–5]. Existing devices, however, are made from materials with substantially different mechanical properties from organs. Previous studies have demonstrated that minimizing stiffness mismatch reduces damage to underlying tissues[5,6], yet currently no arrays exhibit viscous behaviour. Tissues are viscoelastic and undergo permanent deformations with applied stress[7–10]. The importance of substrate viscoelasticity on cell spreading and differentiation has been shown in cell culture[11,12], and the ability of a viscoelastic material to flow and remodel would enhance its conformability to an underlying surface.

Current microfabricated arrays contain electrodes patterned from thin films of metals[6,13]. In addition to a large mechanical mismatch with biological tissues, these metals fracture when subject to large strains. Nanomaterials, such as graphene and carbon nanotubes, have shown promise in the creation of strong yet flexible interfaces with cells[14–17]. When dispersed in hydrogels, the nanocomposites demonstrate a lower mechanical modulus than carbon–elastomers or conductive polymers[18,19]. However, carbon–hydrogel composites are processed on centimetre-scales[20–22] with limited discussion on solvent-free methods for functional integration into microfabricated systems[23,24]. Further, the use of carbon nanomaterials is often limited to electrode coatings[25], and there is minimal adhesion between the conductive hydrogels and the underlying metal tracks. Other nanomaterial systems, such as Ag–Au core–sheath nanowires[26] or Au mesh[27], have demonstrated improved tissue conformability in planar arrays, but still rely on fabrication processes not compatible with etching for precise patterning. Additionally, the electrical components are embedded in plastic or elastic encapsulation layers and hydrogels.

We propose here a class of electrically conductive materials composed of an ultrasoft viscoelastic hydrogel matrix loaded with conductive carbon nanomaterials. Highly porous gels require a low amount of carbon nanomaterials to achieve percolation while retaining a mechanical profile that matches biological tissues. Further, we have fabricated fully viscoelastic arrays by surrounding the tracks with electrically insulating viscoelastic encapsulation layers (Fig. 1a). These viscoelastic arrays plastically deform to allow conformation to the complex geometry of soft tissues.

## Viscoelastic material compatibility with biological tissue

The mechanical properties of fresh lamb brain and rat heart were first characterized as representative tissues to which the devices would be applied (Fig. 1b). Alginate hydrogels[28] with varying levels of crosslinking agent were then analysed to match the viscoelastic properties of the tissues (Fig. 1c and Supplementary Fig. 1). Alginate hydrogels exhibit nanoscale mesh sizes[28], and the surface tension ensures good contact with hydrophilic materials.

To study how mechanical properties impact tissue conformability, substrates of plastic (polyimide), elastic (Ecoflex) and viscoelastic (alginate) materials with comparable bending stiffness (Supplementary Table 1) were placed on a mock porcine brain made of agarose (Supplementary Fig. 2). The polyimide did not conform to the underlying mock brain, whereas the Ecoflex exhibited modest conformability. In contrast, the alginate conformed intimately around the site of placement (Fig. 1d). The alginate substrates

[1]Harvard Program in Biophysics, Harvard University, Cambridge, MA, USA. [2]Harvard–MIT Division in Health Sciences and Technology, Massachusetts Institute of Technology, Cambridge, MA, USA. [3]Wyss Institute for Biologically Inspired Engineering, Harvard University, Cambridge, MA, USA. [4]Laboratory for Soft Bioelectronic Interfaces, Institute of Microengineering, Institute of Bioengineering, Centre for Neuroprosthetics, École Polytechnique Fédérale de Lausanne, Geneva, Switzerland. [5]John A. Paulson School of Engineering and Applied Sciences, Harvard University, Cambridge, MA, USA. [6]Institute for Bioengineering of Catalonia, Barcelona, Spain. [7]Department of Chemistry, The University of Manchester, Manchester, UK. [8]Nanomedicine Lab, National Graphene Institute and Faculty of Biology, Medicine & Health, The University of Manchester, Manchester, UK. [9]Catalan Institute of Nanoscience and Nanotechnology (ICN2), Bellaterra, Barcelona, Spain. ✉e-mail: mooneyd@seas.harvard.edu

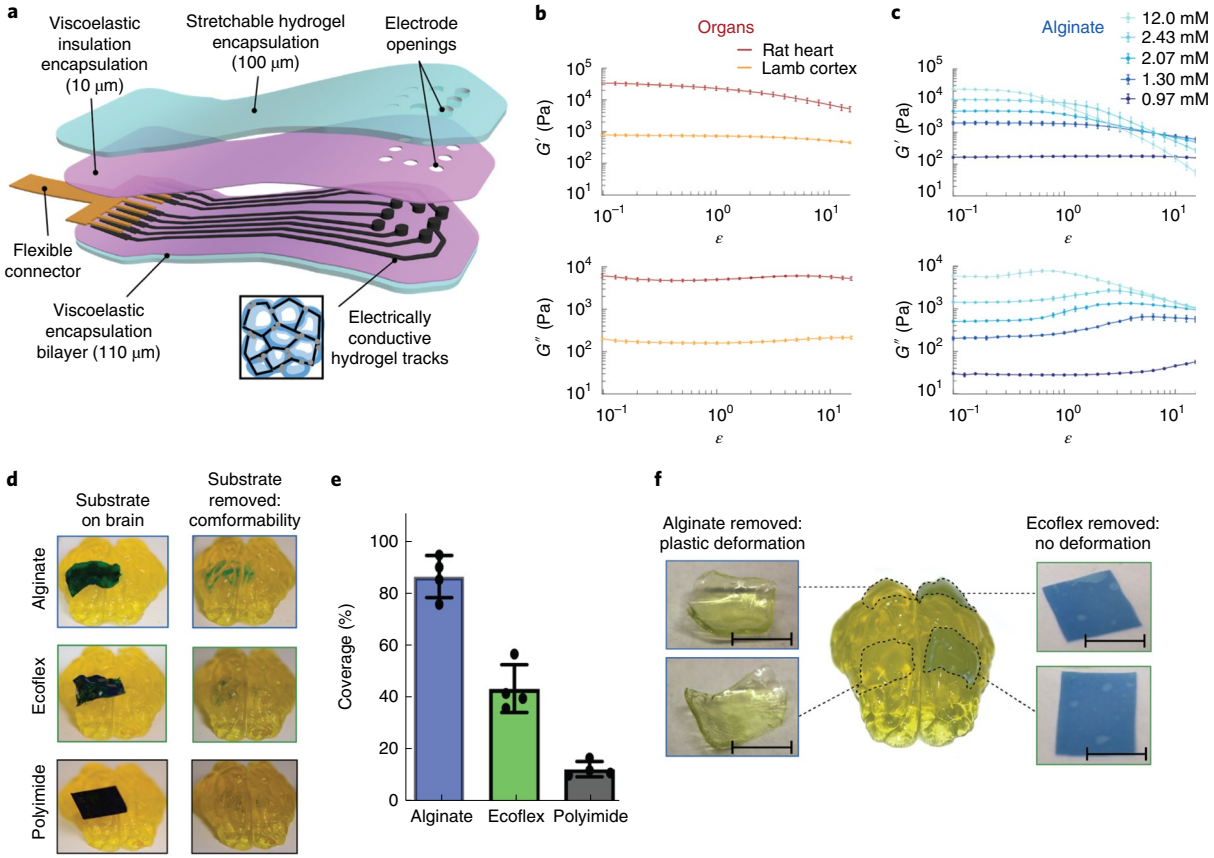


**Fig. 1 | Alginate hydrogels match the viscoelastic properties of mammalian tissues and conform to complex substrates. a**, Schematic of the proposed device and its various components. The encapsulation layer is made from a stretchable hydrogel (blue) to which a viscoelastic electrically insulating polymer (pink) is covalently coupled. The conductive tracks (black) are fabricated from a macroporous hydrogel with carbon additives (inset) and interface with a flexible connector (gold). As all the components of the device are viscoelastic, the assembled array can be designed to match the modulus, and flow to conform to the tissue on which it is implanted. **b**, Rheological properties of fresh lamb cortical tissue and fresh rat cardiac tissue. Storage moduli ($G'$; top) and loss moduli ($G''$; bottom) are shown as a function of strain ($\varepsilon$) at a frequency of 1 Hz for $n = 10$ independent tissue sample sections. The mean and s.d. are plotted. **c**, Rheological properties of alginate hydrogels with varying levels of crosslinking agent, indicated in the legend. Storage moduli ($G'$; top) and loss moduli ($G''$; bottom) are shown as a function of $\varepsilon$ at a frequency of 1 Hz for $n = 8$ independent gels of each formulation. The mean and s.d. are plotted. **d**, Photographs of plastic (5 mm × 15 mm × 25 μm sheet of polyimide; bottom), elastomer (5 mm × 15 mm × 100 μm sheet of Ecoflex; middle) and viscoelastic (5 mm × 15 mm × 250 μm sheet of alginate; top) substrates, with the thickness adjusted so that the bending stiffnesses were comparable. The substrates were coated with blue dye prior to application, and the images demonstrate the shapes adopted by each material immediately following placement on an agarose brain model (left) and after removal of the substrate (right); the dye is transferred from each substrate to the regions of tissue in close contact. **e**, Quantification of the area on the model brains to which dye was transferred for each material (viscoelastic, elastic and plastic), as a metric of the direct contact between the substrates and the porcine brain models. The values are normalized to that of the viscoelastic alginate substrate ($n = 4$ substrates of each material). The mean and s.d. are plotted. **f**, Photographs of viscoelastic (alginate sheets, 5 mm × 5 mm × 200 μm) and elastic (Ecoflex sheets, 5 mm × 5 mm × 100 μm) substrates, both on the porcine brain model and immediately after removal. The two substrates had matching bending stiffness and were placed on the brain models for 2 weeks prior to removal and immediate imaging. Scale bars, 5 mm.

exhibited a twofold increase in contact as compared with the other substrates (Fig. 1e). In addition, the alginate substrates conformed to many of the sulci of the brain. This assay was repeated using biological tissue instead of a mock brain, yielding similar results (Supplementary Fig. 3).

The ability of the elastomeric and viscoelastic substrates to maintain contact over time without damaging the underlying mock tissue was subsequently compared. After placement on mock brains for 2 weeks, the alginate substrates had maintained their original locations, whereas the Ecoflex films had moved substantially and delaminated from the brain surface (Supplementary Fig. 4). Neither substrate resulted in notable tissue compression, likely due to the low bending stiffness of the substrates. Further, the Ecoflex film geometry was unchanged, as compared with its initial shape, upon removal. However, the alginate gel had plastically deformed to match the underlying geometry of both the posterior (smaller radius of curvature) and anterior (larger radius of curvature) portions of the brain (Fig. 1f). An hour post-removal, the alginate had started to return to its initial shape (Supplementary Fig. 5), and after 24 h it had recovered to its original dimensions. If a second gel was placed on top of the deformed gel, the recovery time was reduced to 3 h. The alginate substrate underwent over seven cycles of conformation and relaxation with no impact on the substrate.

Finally, neural cells were seeded on gels with low and high storage moduli (soft vs stiff) and less and more viscoelastic gels (LVEG vs MVEG; Supplementary Fig. 6). The astrocytes were larger on LVEG with a higher cytoplasmic-to-nuclear ratio, resembling activated astrocytes on a control of tissue-culture plastic (TC), as compared

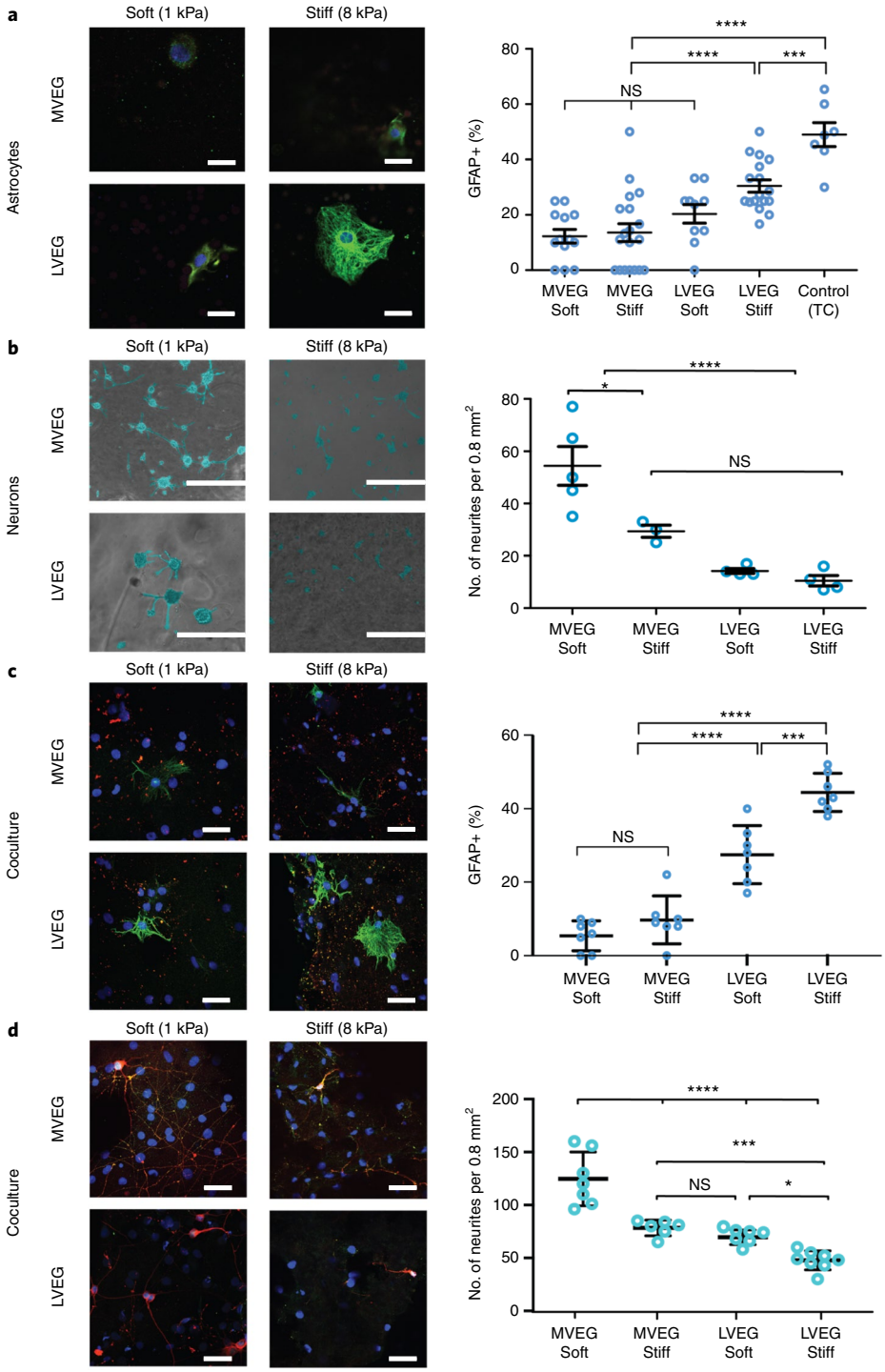


**Fig. 2 | Alginate hydrogels can be tuned to optimize compatibility with both astrocytes, neurons and a coculture. a**, Photomicrographs of primary cortical astrocytes seeded on gels of different viscoelasticity (MVEG, LVEG) and stiffness (soft, stiff) recorded after 120 h (left) and compared with a control of tissue culture plastic (TC). Cells were stained for GFAP (green) and nuclei (blue). Scale bars, 10 μm. Quantification of % cells positive for GFAP on each substrate (right; $n = 4$ per sample, 14 random fields per sample; $P(***) = 0.0021$). **b**, Photomicrographs of primary cortical neurons seeded on RGD-alginate–Matrigel IPNs of different viscoelasticity (MVEG, LVEG) and stiffness (soft, stiff) recorded after 72 h (left). Cell bodies and neurites are falsely coloured blue to provide better contrast from the underlying gel. Scale bars, 400 μm. Quantification of the number of neurites in an area of 0.8 mm$^2$ (right; $n = 4$ per sample, 5 random fields per sample; $P(*) = 0.0194$). **c**, Photomicrographs of a coculture of primary cortical astrocytes and primary cortical neurons seeded on RGD-alginate–Matrigel IPNs of different viscoelasticity (MVEG, LVEG) and stiffness (soft, stiff) recorded after 120 h (left). Cells stained for GFAP (green), MAP2 (red) and nuclei (blue). Scale bars, 40 μm. Quantification of % cells positive for GFAP on each substrate (right; $n = 4$ per sample, 8 random fields per sample; $P(***) = 0.0018$). **d**, Photomicrographs of a coculture of primary cortical astrocytes and primary cortical neurons seeded on RGD-alginate–Matrigel IPNs of different viscoelasticity (MVEG, LVEG) and stiffness (soft, stiff) recorded after 120 h (left). Cells stained for NeuN (green), β3-tubulin (red) and nuclei (blue). Scale bars, 40 μm. Quantification of the number of neurites in an area of 0.8 mm$^2$ (right; $n = 4$ per sample, 7 random fields per sample; $P(*) = 0.0238$; $P(***) = 0.0035$). All numerical data are presented as mean ± s.d. (one-way analysis of variance (ANOVA) and Tukey's honestly significant difference (HSD) post hoc test: $****P < 0.0001$, $0.0001 < ***P < 0.001$, $0.001 < **P < 0.01$, $0.01 < *P < 0.05$, non-significant (n.s.) $P > 0.05$).

with cells on MVEG. The viscoelasticity appeared to play a more important role than the magnitude of the elastic modulus in the cell response (Supplementary Fig. 7). Additionally, a larger fraction of astrocytes on stiff LVEG stained positive for glial fibrillary acidic protein (GFAP+), a marker for astrocyte activation or injury, compared with the cells on either MVEG (Fig. 2a and Supplementary Fig. 8). Similar studies were performed with neurons using RGD-alginate–Matrigel interpenetrating networks (IPNs)[7] of varying stiffness and viscoelasticity (Supplementary Fig. 9). Primary neurons were found to extend significantly farther and give a higher density of neurites on soft MVEG gels (Fig. 2b), and stiff MVEG gels exhibited the next most expansive neurite network. Repeating these studies with a coculture of primary astrocytes and primary neurons led to similar findings (Fig. 2c,d and Supplementary Figs. 10 and 11).

## An ultrasoft, highly porous conductive hydrogel

Next, electrically conductive gel-based interconnects were fabricated from the soft MVEG alginate hydrogels. To enhance the limited intrinsic ionic conductivity of the alginate, both pyrene-modified defect-free graphene flakes (GFs; Supplementary Methods and Supplementary Fig. 12) and carbon nanotubes (CNTs) were added. These high aspect ratio carbon-nanomaterial additives were suspended in the alginate prior to gelation (Fig. 3a), and microporous gels were fabricated by freezing the gels before crosslinking to reduce the percolation threshold of the conductive particles. Both the nanoporous conductive gels (nanoCGs; no freezing before crosslinking) and microporous conductive gels (microCGs) were cast in moulds, resulting in tracks that could conform to the complicated geometries of the sulci and vasculature (Fig. 3b). The tracks were bent >180°, tied into knots without breaking and remained in situ for multiple days without damage (Supplementary Fig. 13). No swelling was observed in either the nanoCGs or the microCGs, and there were no changes to the electrodes nor track features over time as the conductive gels cycled between conforming to an underlying tissue and relaxing to their original shape.

Scanning electron microscopy (SEM) revealed that the inclusion of GFs and CNTs altered the structure of both the nanoCG and microCG (Fig. 3c). In the nanoCG, the surface roughness increased with more additives, and larger particle aggregates were apparent with higher quantities of carbon nanomaterials. GFs were integrated into the walls of the microCG, whereas the CNTs formed dense nodes throughout the microCG. When both were present in the microCG, the GFs appeared to connect to the CNT bundles, improving the probability of a percolating path. The microCG wall thickness was between 750 and 850 nm, which is smaller than the length of the CNTs and allowed CNTs to span multiple pores. The resulting high surface area of the microCG is likely to be advantageous for interfacing with neurons.

The electrical behaviours of the nanoCG and microCG were subsequently studied using four-point probe resistance for gels that were 100 µm thick (Supplementary Fig. 14), and conductivity values were compared for gels containing only GFs (Fig. 3d), only CNTs (Fig. 3e) and a combination of GFs and CNTs (GF + CNT; Fig. 3f). For all cases, the microCG formulations were significantly more conductive than the nanoCG equivalents. Conductivity values greater than 10 S m$^{-1}$, and as high as 35 S m$^{-1}$, could be achieved with microCG compositions with less than 2% carbon-nanomaterial loading (Fig. 3e,f). The microCG reached the percolation threshold at ~0.9% carbon (Fig. 3g), with a residual fitting parameter of $R^2 = 0.89$. To explore the relative electrical contribution of each additive in the microCG, conductivity was plotted (by colour) as a function of both GF and CNT content (Fig. 3h). The conductivity tended to increase with the amount of carbon additive, but increased more substantially with rising CNT content (region I) than with increasing GFs (region II). The conductivity increased faster and had less variability in GF + CNT gels (region III). SEM images revealed that as more carbon was added, the total porosity of the gels was not significantly affected (Supplementary Fig. 15), but the distribution of pore size seemed to increase (Fig. 3i).

The various gel compositions were assessed to determine how added carbon nanomaterials impacted their mechanical properties. Rheological analysis revealed that bulk gel $G'$ and $G''$ were not affected in a statistically significant manner as carbon was varied from 0 to 1.4% (Supplementary Fig. 16), and nanoindentation analysis of the surface mechanical properties also indicated that neither $G'$ (Fig. 3j) nor $G''$ (Fig. 3k) was statistically altered in microCGs containing 0–2% carbon. These measurements had a large standard deviation, and the nanoindenter tip could have been in contact with the wall or strut of the gel, a more porous area, or a region that could have been more/less rich with carbon-nanomaterial additives. The range presented here is more similar to the mechanics of heterogeneous tissues than other reported conductive composites, and the conductive components are in contact with the underlying tissue only at the electrode sites. Further, the conductive gels had no detrimental impact on the viability of exposed astrocytes (Supplementary Fig. 17).

## Fabrication of a viscoelastic encapsulation layer

A process to fabricate a viscoelastic encapsulation layer was next developed. As the encapsulation layer must electrically insulate each electrical track, and the ionically crosslinked

**Fig. 3 | Viscoelastic electronics formed from an alginate matrix with electrically active carbon-based fillers. a**, Schematic showing the fabrication of nanoCGs and microCGs. An alginate solution, GFs and/or CNTs were mixed and immediately crosslinked to create nanoCGs (pore diameter, approx. tens of nanometres; top). When the mixed solution was frozen and lyophilized before crosslinking, microCGs (pore diameter, approx. hundreds of micrometres) were formed with a higher density of carbon additives in the gel walls (bottom). RT, room temperature. **b**, Photographs demonstrating the casting of the tracks in a flexible mould (left), and their ability to follow the vasculature of a fresh lamb brain (right). Scale bars, 10 mm. **c**, SEM photomicrographs comparing nanoCGs (top row; scale bars, 100 µm) and microCGs (middle row; scale bars, 50 µm) with no additives, only GFs, only CNTs and with GF and CNT. Higher magnification images of the microCGs are also shown (bottom row; scale bars, 5 µm). Red arrows point to CNTs, and red asterisks indicate regions containing GFs. **d**–**f**, Quantification of the conductivity of nanoCGs and microCGs, comparing the behaviour of gels with GF-only (**d**), CNT-only (**e**) and GF + CNT (**f**) compositions with increasing concentrations of carbon ($n = 38$ independent gels). Error bars (s.d.) are shown in black; all $P(****) < 0.0001$. **g**, Quantification of the conductivity of microCGs as a function of total carbon (GF + CNT) composition, fitted with a sigmoidal curve ($R^2 = 0.89$). **h**, Graphical evaluation of the relative contribution of GFs and CNTs to the conductivity of the microCGs. The resulting gel conductivities, ranging from low (blue) to high (red) conductivity, are indicated by the colour bar. I, II and III mark regions of mostly CNTs, mostly GFs and a mix of GF + CNT, respectively. Each small solid circle represents an independent gel measurement, and the colour of each grouping of solid circles represents the mean conductivity ($n = 20$–$30$ per composition). **i**, SEM photomicrographs comparing the structures of microCGs at varying concentrations of only CNTs, only GFs and a mix of GF + CNT. I (purple), II (red) and III (green) mark regions of mostly CNTs, mostly GFs and a mix of GF + CNT, respectively. Scale bars, 20 µm. **j**,**k**, Quantification of the storage modulus ($G'$; **i**) and loss modulus ($G''$; **j**) of GF + CNT microCGs using nanoindentation analysis ($n = 10$ independent gels). All conditions were n.s. All numerical data are presented as mean ± s.d. (one-way ANOVA and Tukey's HSD post hoc test: $****P < 0.0001$, n.s. $P > 0.05$). Micrographs were collected from at least three independent gels.

alginate gels themselves do not provide electrical insulation, a thin (15 µm) layer of an insulating physically entangled viscoelastic material (PEVM) was covalently attached to a thicker (100 µm) alginate-based tough gel (TG)[29] with similar viscoelasticity as the alginate-only gels (Supplementary Fig. 18) such that the TG portions were the outermost layers and in direct contact with the tissue (Fig. 4a). The insulation layer is based on a previously reported self-healing polydimethylsiloxane (PDMS)[30] that was physically entangled with amine-terminated PDMS to provide surface-exposed amine groups to conjugate to the surface carboxy groups of the TG (Supplementary Fig. 19). The resulting bilayers were highly deformable, as they could be strained to 1,000% (Fig. 4b) and had an effective elastic modulus ($E$) that was almost 20-fold less than that of pure PEVM films, and only slightly larger than that of the TG alone (Fig. 4c). These encapsulation materials had no detrimental impact on astrocyte viability (Supplementary Fig. 17), and could be patterned with a $CO_2$ laser to create openings at the desired electrode sites without compromising the attachment process of the bilayer. The patterned encapsulation layers could also be stretched without tearing at the interface of the patterned portions (Fig. 4d).

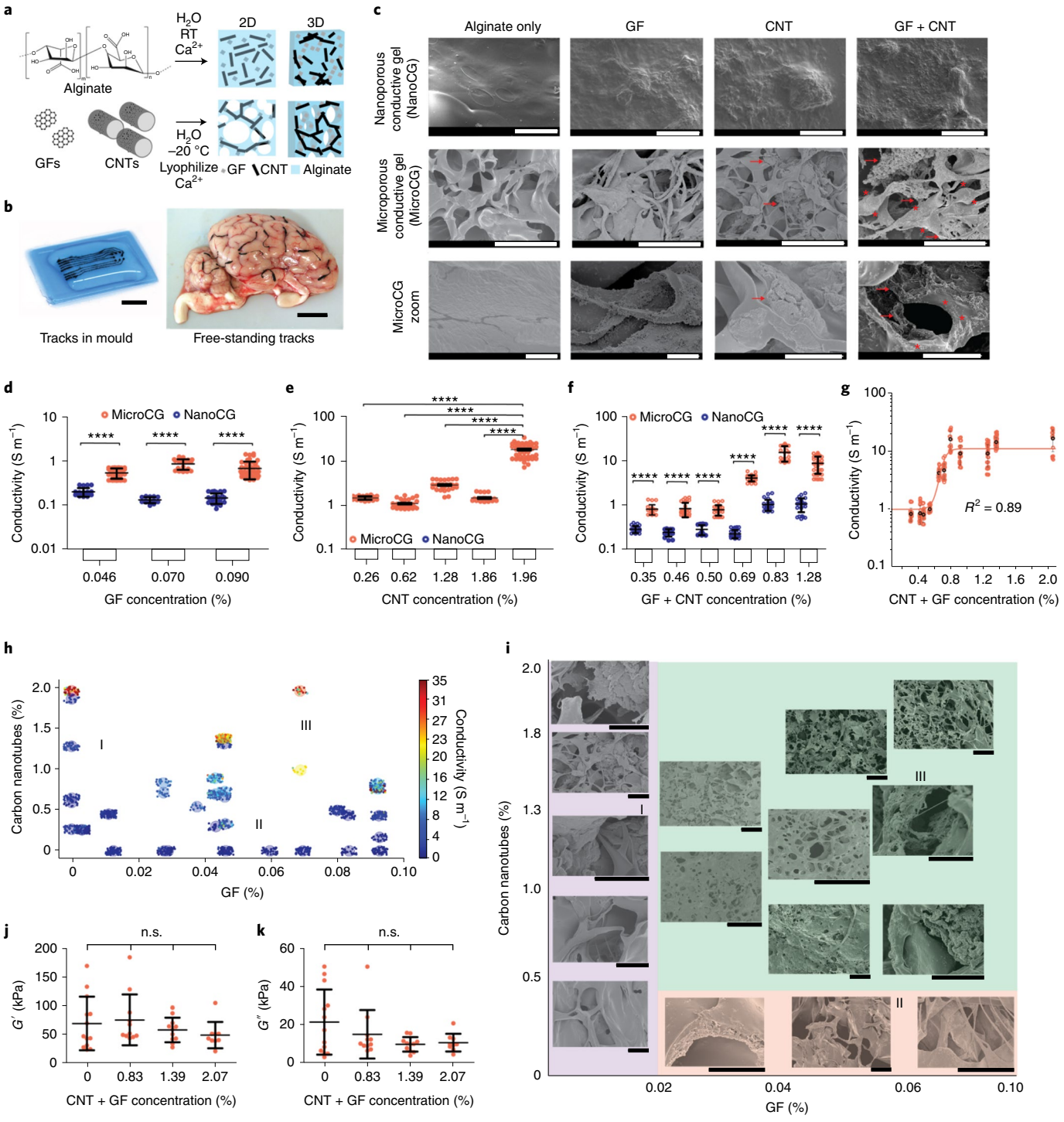

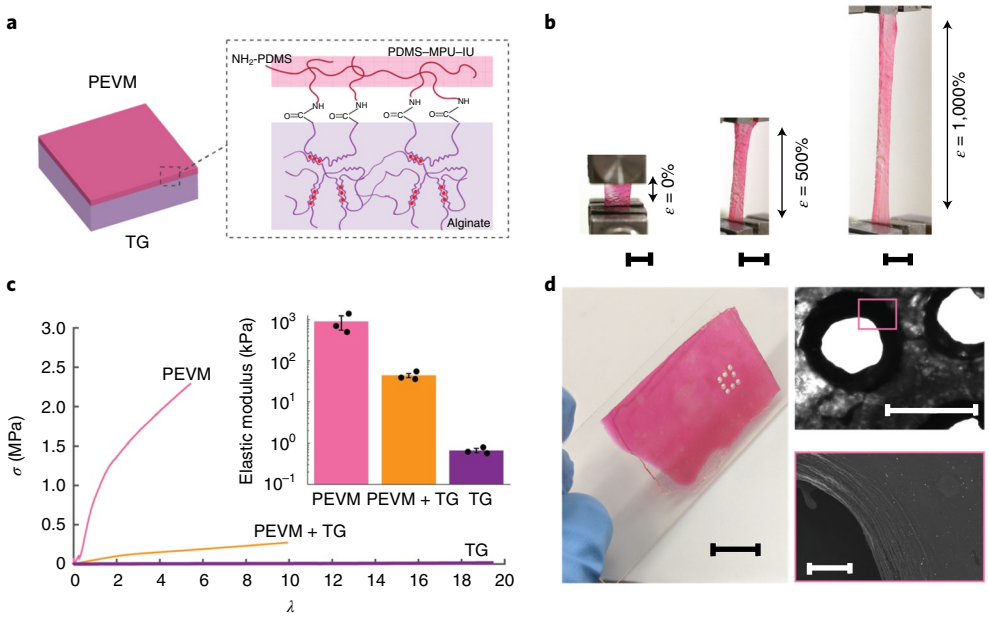


**Fig. 4 | Fabrication of highly flexible and stretchable viscoelastic encapsulation layers. a**, Schematic of the two individual components that comprise the encapsulation layers of the device. A stretchable alginate TG (purple) was covalently coupled to a self-healing, PDMS-based PEVM (pink) through carbodiimide chemistry. **b**, Photographs of the composite encapsulation layer stretched under tension to 0, 500 and 1,000% of the original length. The PEVM (pink) can be observed to begin to fracture under the greatest strain, while the TG (clear) remained intact. Scale bars, 5 mm. **c**, Quantification of the stress ($\sigma$) versus elongation ($\lambda$) behaviour of the encapsulation materials until the first point of film fracture. A representative curve is shown for each encapsulation layer tested: PEVM-only, TG-only and PEVM–TG. Inset: the elastic modulus for each material was extracted from the linear regime. Values in the inset represent the mean and s.d. ($n = 3$ independent materials for each condition). **d**, Photographs of the encapsulation layer following cutting with a $CO_2$ laser (left), and bright-field microphotograph (right, top) and SEM image (right, bottom) of the cut after exposure to the laser. Scale bars, 10 mm (left), 1 mm (right, top) and 100 μm (right, bottom).

## Assembly of fully viscoelastic devices and in vivo validation

The process to fabricate fully viscoelastic arrays is described in Supplementary Fig. 20. The self-healing properties of the PEVM enabled seamless integration of the two PEVM layers through hydrogen bonding. The completed devices were viscoelastic and highly conformable (Fig. 5a). Further, the conductive tracks could be fabricated with stiffness and viscoelasticity that overlap with those of heart and brain tissue (Fig. 5b)[18,31–39]. This contrasts with previously described electrical composites, which typically have much higher moduli and do not exhibit the viscoelasticity of tissues.

The electrical behaviour of the fabricated devices was first characterized in phosphate buffer solution (PBS). The composite was cast in moulds with deeper electrode sites, and a flexible comb-like connector was used to intimately contact each pad. The median impedance range at 1 kHz for 5 devices with 40 tracks was $167 \pm 40$ kΩ, with an electrode surface area of 0.38 mm$^2$ (Fig. 5c). The intertrack resistance was 2–40 MΩ in a hydrated environment, confirming that there were no short circuits between independent tracks (Supplementary Fig. 21).

Impedance spectra at 1 kHz and the intertrack resistance of four arrays were measured over time following submergence in PBS with 2 mM $CaCl_2$ for 84 days at room temperature (Fig. 5d). Three of the arrays showed no significant change in impedance, and the intertrack resistance did not significantly change for any of the arrays. Further, all devices remained fully attached and with no changes in any dimensions. To mimic the effects of multiaxial mechanical cycling in a physiological system, a mouse was intubated and mechanically ventilated with the stroke volume set to correspond to 11% linear strain in each direction, similar to the physiological strain experienced by the mouse heart. An array was placed on the exposed muscle and cycled either 10,000 or 100,000 times (Fig. 5e). All 24 electrodes cycled 10,000 times showed less than a twofold increase in impedance. For the array cycled 100,000 times, only one electrode visibly fractured. No array slipped, as the hydrogel encapsulation was intimately interfaced with the hydrophilic tissue.

The viscoelastic array was fabricated to match the dimensions of a commercial array, and the conformability and functionality of the two were compared on a bovine heart (Fig. 5f). When both arrays were placed on a flat portion of the tissue, all four electrodes made good contact and demonstrated a consistent impedance (105 kΩ and 300 Ω for the viscoelastic and commercial electrodes, respectively). On the heart wall, on which the arrays needed to bend by more than 90°, none of the electrodes of the commercial grid was in contact with the tissue. However, all four electrodes of the viscoelastic grid remained in contact and experienced no significant change in the impedance (Supplementary Fig. 22). Further, when bent by >180° around the tissue, the viscoelastic array remained in contact, with no change in the functionality (Supplementary Fig. 23). The charge storage capacity (CSC) of the clinical-scale grids (electrode diameter, 5 mm) was calculated over the voltage range corresponding to the water window for each composition (Fig. 5g), and the carbon-based electrodes showed tenfold more CSC than the platinum electrodes. This voltage range was −4 to 4 V for the nanomaterial electrodes and −1 to 1 V for the platinum electrodes, as the carbon tracks are highly resistive and thus required a higher applied voltage to reach water electrolysis at the electrode interface. As the relative ratios of the GFs and CNTs were modified, the CSC changed, which suggests that the composition of the carbon additive can be tuned to achieve stimulation electrodes or recording electrodes (Supplementary Fig. 24).

Arrays were placed on explanted tissues and were observed to conform to the cortical surface of a rat brain, intimately covered a rat heart and precisely wrapped around nerves in a bovine heart

(Fig. 6a). There was no macroscopic damage caused to any of the structures, and no array components delaminated. To validate the functionality in vivo, a mouse hindlimb was stimulated at various locations (Fig. 6b). The pulse parameters were kept constant, but the location of the electrode or the electrode which applied the stimulation were changed. This resulted in different responses, such as activation of the toes only, the ipsilateral foot only, the entire ipsilateral ankle or both the ipsilateral and contralateral limbs (Supplementary Videos 1 and 2 show toe and foot activation, respectively).

Finally, we evaluated the recording capabilities of the viscoelastic array on the heart and brain of rodents. During acute in vivo surgeries, arrays were placed on the epicardial surface of a mouse heart or on the epidural surface of a rat cortex. An eight-electrode array, as a 3 × 3 grid of electrodes with a diameter of 700 µm and a spacing of 800 µm between adjacent electrodes and with the centre position left empty, was designed for these studies; larger arrays and more electrodes can be readily fabricated for studies with larger animals. The array stayed flat on the mouse heart and remained in place as a result of surface tension and plastic deformation as the organ continued to beat (Supplementary Fig. 25). We recorded electrocardiograms (ECGs; Fig. 6c) with a maximum signal-to-noise ratio (SNR) of 17.4. Next, the array was wrapped around the heart and ECGs were recorded from the posterior side of the tissue, with the array bent more than 180° (Fig. 6d). The electrodes remained functional, with a SNR of 15.6. To confirm the signals recorded were specific to the heart, and not an artefact from the physical movement of the tissue, the grid was placed on the exposed liver, where no electrical signal was recorded (Supplementary Fig. 26).

For neural recordings, the electrode array was placed on the dura of a Thy1 rat. This transgenic rat model was used as its neurons could be depolarized by directing a blue-light laser beam at the cortex through the transparent portions of the viscoelastic grid (Supplementary Fig. 27). First, the laser at 90 mW power was directed towards the centre of the array, indicated in Fig. 6e, to induce electrical activity in the underlying cortex. All eight electrode channels successfully recorded electrical activity (Supplementary Fig. 28), and the traces over the recording session were averaged for each channel ($n = 63$) and are plotted in Fig. 6e. Signals with an amplitude of approximately 1 mV were recorded, and depolarization events corresponding to the laser stimulation were reliably identified. Next, the laser position was moved to the left-lateral edge, and the amplitude and waveform of the recorded activity were diminished. Thus, the neural activity recorded by the array was significantly reduced when the laser was directed on the lateral portion of the array, and further, the amplitudes of the traces obtained at both laser positions were reduced when the power was lowered to 45 mW. Finally, when the pulse duration of the laser was increased from 5 to 10 ms, the time to electrical depolarization over the electrodes increased, and this trend was observed for three levels of laser power (Supplementary Fig. 29). These experiments confirm that the recorded activity was a real signal based on the underlying neurons, as opposed to non-specific tissue activity. Additionally, the amplitude of the activity recorded is comparable to existing arrays with similar electrode diameters[6,13].

A three-electrode viscoelastic array was also placed over the auditory cortex of a wild-type rat (Fig. 6f). This far-lateral cortical target is surgically more difficult to access, and the device was bent by more than 180°. The array remained functional, and all electrodes recorded auditory evoked potentials (AEPs) in response to tone bursts from 1 to 10 kHz frequency. The three electrodes displayed typical AEPs at the onset and offset of the sound. Interestingly, the relative magnitude of the AEP amplitude at sound onset and offset differed amongst the three electrodes, which suggests that the electrodes were recording local tonotopic information. Indeed, each electrode displayed a different frequency tuning profile with a maximum SNR of 18 for the recorded surface potentials.

## Conclusions

We have reported here the first fully viscoelastic electrode array that exhibits a similar mechanical profile to soft biological tissues. The arrays were prepared mostly from hydrogels, which have highly tuneable physical properties, and the viscoelasticity and stiffness could be independently varied. Additionally, the surface arrays feature novel electrical conductors made from low loading fractions of high aspect ratio carbon nanomaterials, and thus they retained an ultrasoft modulus and viscoelastic nature. Likely due to the matching of the mechanical properties with neural tissue, the neural cell responses to the soft viscoelastic array materials in vitro were favourable, with minimal astrocyte activation and enhanced neurite spreading. Further, high SNR values of 18 were obtained in vivo, enabling the recording of low-amplitude local field potentials. Further, the electrode design and array fabrication process are facile and fast (3 days from design to the functional and fully assembled array) and do not require high temperatures, harsh chemical etchants or thin-film photolithographic technologies. As the electrodes and tracks have the same composition, and due to the stability of the GFs and CNTs, there is no interface delamination or need for metallic films, thus presenting a class of arrays that would be compatible with a multitude of imaging techniques, such as magnetic resonance imaging (MRI). Because different compositions of carbon additives demonstrated tunability of the CSC,

**Fig. 5 | Device characterization and in vitro validation of the fully viscoelastic devices. a**, Photographs of the fully assembled array (6 mm × 20 mm × 250 µm) with eight electrodes of diameter 700 µm and a 1.5 mm pitch, flat in PBS (left) and bent (right). Scale bar, 3 mm. **b**, Quantification of the elastic modulus, conductivity and viscoelasticity (tan($\delta$)) of various tissues and conductive composites. Rat heart and brain tissue, shown in orange, represent the targeted physiological stiffness and viscoelasticity. The alginate-based conductors fabricated in this study are shown in purple. Values for other conductive composites reported in the literature are also represented, using the reported ranges for each variable. Literature citations for the values in the illustration are provided, with the relevant data collected in Supplementary Table 2. **c**, Electrical impedance spectroscopy data of five devices, from five distinct batches, measured in PBS, showing the impedance modulus ($Z$ modulus; top) and impedance phase ($Z$ phase; bottom) over a frequency sweep from 1 MHz to 1 Hz. The mean and s.d. of each device are plotted ($n = 40$ electrodes). **d**, Comparison of the electrode impedance of four arrays at 1 kHz before and after ageing in PBS for 84 days (top). The impedance for each electrode is normalized to the impedance value before ageing. Intertrack resistance between adjacent electrodes, plotted before and after ageing in PBS ($n = 4$ independent devices; bottom). The numerical data are presented as mean ± s.d. (one-way ANOVA and Tukey's HSD post hoc test; $^{*}P < 0.05$ ($P = 0.02$), n.s. $P > 0.05$. **e**, Multiaxial mechanical cycling of the viscoelastic arrays, at 11%-equivalent biaxial strain, with the relative change in impedance ($\Delta Z/Z$) at 1 kHz plotted for each electrode. Three devices were cycled 10,000 times (left) and one device was cycled 100,000 times (right). **f**, Photographs of a commercial clinical grid (pink) with a similar-dimensioned viscoelastic array (blue) on a bovine heart (left). The grids were placed on smooth regions of the tissue (solid line) and bent 90° around the heart (dashed lines). Scale bar, 10 mm. The impedance at 1 kHz was extracted for each electrode ($n = 4$ per device) and the values for the flat and bent configurations are compared (right). The mean and s.d. are plotted. $^{****}P < 0.0001$, n.s. $P > 0.05$. **g**, Cyclic voltammetry of an electrode from a commercial grid and from the viscoelastic array developed in this work. Inset: the bar graph shows the CSC extracted from each electrode ($n = 4$ per device) and compared for four electrodes from each array. The mean and s.d. of each electrode are plotted.

a combination of different formulations could be used to fabricate an array that has some tracks more optimized for stimulation and others more optimized for recording.

This ultrasoft technology can likely be optimized for future application in bioelectronic interfaces, for both two-dimensional (2D) and three-dimensional (3D) microelectrode arrays, and also become a useful tool to better understand how organs develop, function and change throughout diseased states. A striking feature of these viscoelastic arrays is that they plastically deform upon implantation, enabling rapid 'personalization' to the local environment without the need for changing the electrode layout. The same initial 2D grid will quickly conform to the underlying tissue architecture

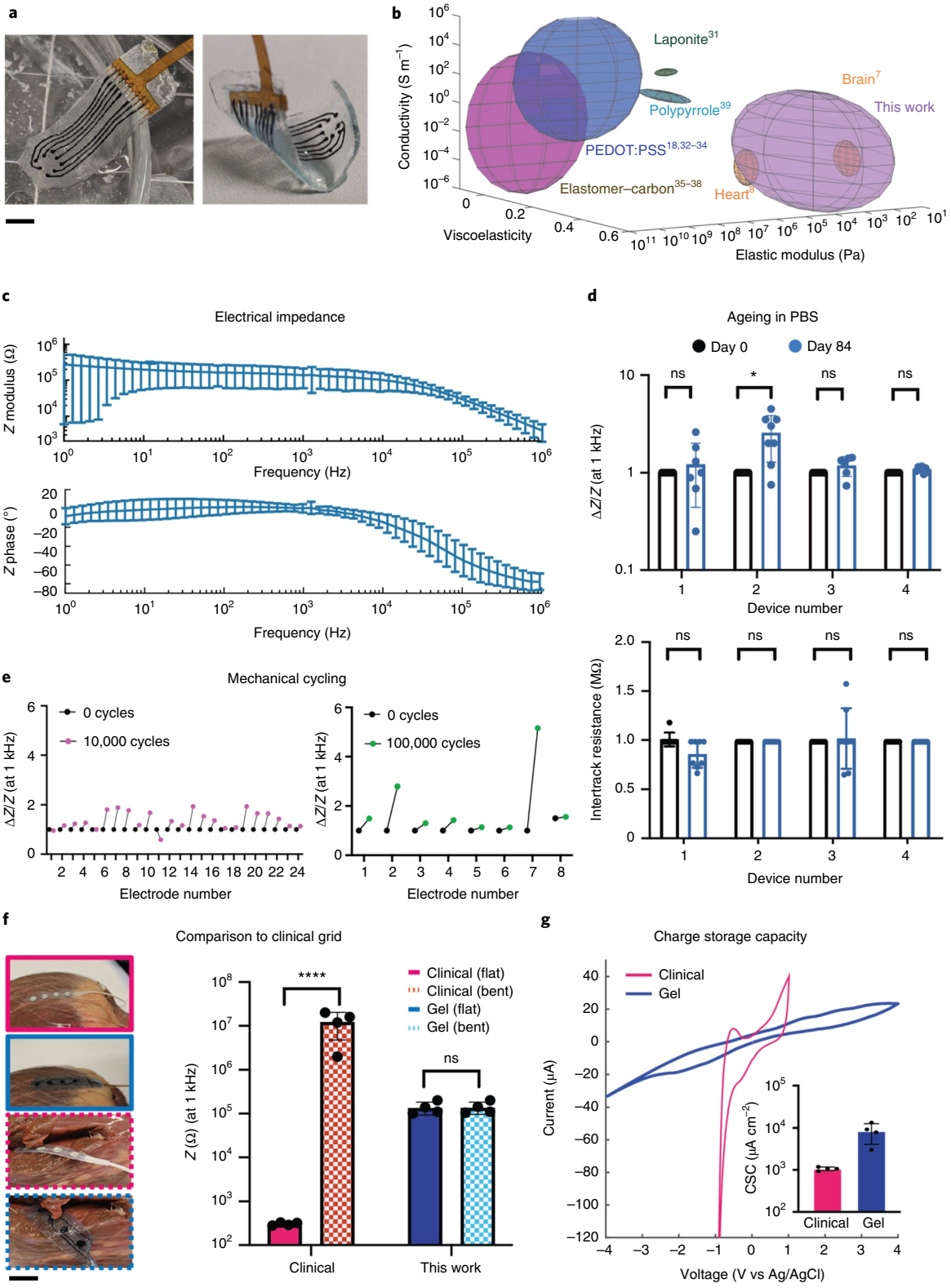

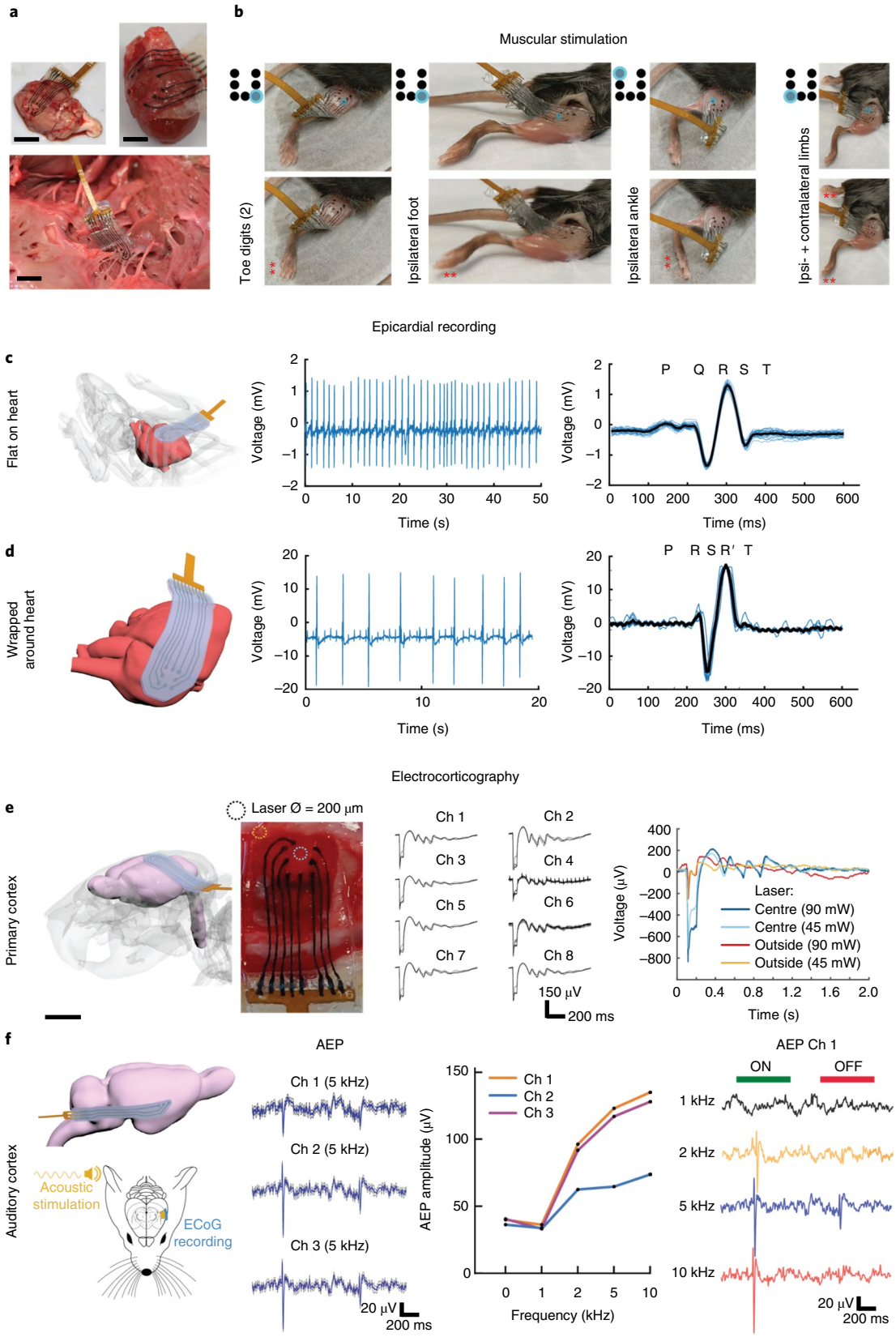


without compromising the electrical and mechanical properties of the nanomaterial-based tracks. Implantation of the arrays in larger mammals, such as the porcine brain, would offer complex geometries (for example, intrasulcular) for recordings, which are currently inaccessible without causing significant plastic damage to the tissue.

As our arrays are currently limited by the track width of the electrodes due to the small anatomy of rodents, the technology would benefit from applications in which the features could be scaled up. This could be done without increasing the overall thickness of the device, nor compromising its viscoelastic nature.

**Fig. 6 | In vivo validation of the fully viscoelastic device for stimulation and for recording, even under extreme deformation. a**, Photographs of the assembled viscoelastic array on a rat cortical surface (top, left), conformed around a rat heart (top, right) and wrapped around the nerves of a bovine heart (bottom). Scale bars, 3 mm. **b**, Photographs, taken from videos, of the viscoelastic array stimulating the exposed muscle of a mouse hindlimb. By positioning the array or changing the electrode applying the stimulation pulses, the toes only (far left), the foot only (left), the ankle (right) or both the contralateral and ipsilateral limbs (far right) were triggered. Red asterisks (**) mark the portion of the limb responding to stimulation. The schematic to the left of each image shows the representative electrode (blue) that is stimulating the tissue. Top row, the limb when not stimulated (at rest); bottom row, the limb at the maximum amount of deflection during stimulation (activated). **c**, Schematic of the viscoelastic array, flat and conformed to the surface of a mouse heart (left). Acute electrical activity recorded in vivo from the mouse heart with three electrodes, showing the filtered ECG (middle) and the superimposed average (black) of all the beats (right). Individual cycles are shown in light blue. The figure was realized thanks to the rat skeleton 3D model shared by Doney et al. (https://3dprint.nih.gov/license/cc)[40]. **d**, Schematic of the viscoelastic array, wrapped almost 360° around the surface of a mouse heart and remaining conformed (left). Acute electrical activity recorded in vivo from the mouse heart with three electrodes, showing the filtered ECG (middle) and superimposed average (black) of all the beats (right). Individual cycles are shown in light blue. **e**, Schematic of the viscoelastic array placed on the cortical surface of a rat brain (far left). Photograph of the viscoelastic array on top of the exposed dura of a Thy1 rat cortex (scale bar, 4 mm), with circles added to show where stimulation by a laser was applied (either in the blue circle, at the centre of the device, or in the brown circle, on the lateral edge of the device; left). Acute electrical activity recorded in vivo, epidurally from the cortical surface after stimulation by a blue-light laser, at the centre or lateral edge of the array. The depolarization for each electrode channel (Ch) is shown by the respective electrode trace, as the average and standard deviation over the recording session (right). Comparison of the electrical activity recorded by a single channel as the laser position was moved from the centre of the device to the lateral edge, and as the laser power was changed from 90 mW to 45 mW (far right). The figure was realized thanks to the rat brain 3D model shared by Pohl et al. (figshare: https://doi.org/10.6084/m9.figshare.823546.v1). **f**, Schematic of the viscoelastic array, bent by more than 90° to reach the auditory cortex of a rat brain (top, far left). Schematic of the set-up for recording from the auditory cortex (bottom, far left). ECoG, electrocorticogram. Acute electrical activity recorded in vivo, epidurally from the auditory cortical surface from each of the three electrodes (Ch) of the array when an acoustic tone of 5 kHz was applied (left). In addition to recording AEPs from each channel, an independent frequency tuning profile of each channel was obtained (right). Tone burst stimulation (duration of 1 s) was performed, and the AEPs from Ch 1 were recorded for four applied acoustic tones (1, 2, 5 and 10 kHz; far right). 'ON' and 'OFF' of the tone burst are indicated above the AEP traces.

## Online content

Any methods, additional references, Nature Research reporting summaries, source data, extended data, supplementary information, acknowledgements, peer review information; details of author contributions and competing interests; and statements of data and code availability are available at https://doi.org/10.1038/s41565-021-00926-z.

Received: 30 September 2020; Accepted: 5 May 2021;
Published online: 17 June 2021

## References

1. Tolstosheeva, E. et al. A multi-channel, flex-rigid ECoG microelectrode array for visual cortical interfacing. *Sensors (Basel)* **15**, 832–854 (2015).
2. Luan, L. et al. Ultraflexible nanoelectronic probes form reliable, glial scar–free neural integration. *Sci. Adv.* **3**, e1601966 (2017).
3. Tybrandt, K. et al. High-density stretchable electrode grids for chronic neural recording. *Adv. Mater.* **30**, e1706520 (2018).
4. Konerding, W. S., Froriep, U. P., Kral, A. & Baumhoff, P. New thin-film surface electrode array enables brain mapping with high spatial acuity in rodents. *Sci. Rep.* **8**, 1–14 (2018).
5. Lacour, S. P., Courtine, G. & Guck, J. Materials and technologies for soft implantable neuroprostheses. *Nat. Rev. Mater.* **1**, 16063 (2016).
6. Minev, I. R. et al. Electronic dura mater for long-term multimodal neural interfaces. *Science* **347**, 159–163 (2015).
7. Chaudhuri, O. et al. Extracellular matrix stiffness and composition jointly regulate the induction of malignant phenotypes in mammary epithelium. *Nat. Mater.* **13**, 970–978 (2014).
8. Budday, S. et al. Region- and loading-specific finite viscoelasticity of human brain tissue. *Proc. Appl. Math. Mech.* **18**, 3–4 (2018).
9. Wang, Z., Golob, M. J. & Chesler, N. C. in *Viscoelastic and Viscoplastic Materials* (InTech: 2016); https://doi.org/10.5772/64169
10. Boyle, N. G. & Shivkumar, K. Epicardial interventions in electrophysiology. *Circulation* **126**, 1752–1769 (2012).
11. Chaudhuri, O. et al. Substrate stress relaxation regulates cell spreading. *Nat. Commun.* **6**, 6365 (2015).
12. Chaudhuri, O. et al. Hydrogels with tunable stress relaxation regulate stem cell fate and activity. *Nat. Mater.* **15**, 326–334 (2016).
13. Rubehn, B., Bosman, C., Oostenveld, R., Fries, P. & Stieglitz, T. A MEMS-based flexible multichannel ECoG-electrode array. *J. Neural Eng.* **6**, 036003 (2009).
14. Bramini, M. et al. Interfacing graphene-based materials with neural cells. *Front. Syst. Neurosci.* **12**, https://doi.org/10.3389/fnsys.2018.00012 (2018).
15. Kostarelos, K. & Novoselov, K. S. Graphene devices for life. *Nat. Nanotechnol.* **9**, 744–745 (2014).
16. Martín, C., Kostarelos, K., Prato, M. & Bianco, A. Biocompatibility and biodegradability of 2D materials: graphene and beyond. *Chem. Commun.* **55**, 5540–5546 (2019).
17. Pampaloni, N. P., Giugliano, M., Scaini, D., Ballerini, L. & Rauti, R. Advances in nano neuroscience: from nanomaterials to nanotools. *Front. Neurosci.* **12**, 953 (2019).
18. Lu, B. et al. Pure PEDOT:PSS hydrogels. *Nat. Commun.* **10**, 1043 (2019).
19. Liu, Y. et al. Morphing electronics enable neuromodulation in growing tissue. *Nat. Biotechnol.* **38**, 1031–1036 (2020).
20. Yuan, X., Wei, Y., Chen, S., Wang, P. & Liu, L. Bio-based graphene /sodium alginate aerogels for strain sensors. *RSC Adv.* **6**, 64056–64064 (2016).
21. Golafshan, N., Kharaziha, M. & Fathi, M. Tough and conductive hybrid graphene-PVA: alginate fibrous scaffolds for engineering neural construct. *Carbon* **111**, 752–763 (2017).
22. Lin, X. et al. A viscoelastic adhesive epicardial patch for treating myocardial infarction. *Nat. Biomed. Eng.* **3**, 632–643 (2019).
23. Son, D. et al. An integrated self-healable electronic skin system fabricated via dynamic reconstruction of a nanostructured conducting network. *Nat. Nanotechnol.* **13**, 1057–1065 (2018).
24. Masvidal-Codina, E. et al. High-resolution mapping of infraslow cortical brain activity enabled by graphene microtransistors. *Nat. Mater.* **18**, 280–288 (2019).
25. Green, R. Elastic and conductive hydrogel electrodes. *Nat. Biomed. Eng.* **3**, 9–10 (2019).
26. Choi, S. et al. Highly conductive, stretchable and biocompatible Ag–Au core–sheath nanowire composite for wearable and implantable bioelectronics. *Nat. Nanotechnol.* **13**, 1048–1056 (2018).
27. Lee, S. et al. Ultrasoft electronics to monitor dynamically pulsing cardiomyocytes. *Nat. Nanotechnol.* **14**, 156–160 (2019).
28. Lee, K. Y. & Mooney, D. J. Alginate: properties and biomedical applications. *Prog. Polym. Sci.* **37**, 106–126 (2012).
29. Sun, J. Y. et al. Highly stretchable and tough hydrogels. *Nature* **489**, 133–136 (2012).
30. Kang, J. et al. Tough and water-insensitive self-healing elastomer for robust electronic skin. *Adv. Mater.* **30**, e1706846 (2018).
31. Tondera, C. et al. Highly conductive, stretchable, and cell-adhesive hydrogel by nanoclay doping. *Small* **15**, 1901406 (2019).
32. Kim, N. et al. Elastic conducting polymer composites in thermoelectric modules. *Nat. Commun.* **11**, 1424 (2020).
33. Wang, Y. et al. A highly stretchable, transparent, and conductive polymer. *Sci. Adv.* **3**, e1602076 (2017).

34. Feig, V. R., Tran, H., Lee, M. & Bao, Z. Mechanically tunable conductive interpenetrating network hydrogels that mimic the elastic moduli of biological tissue. *Nat. Commun.* **9**, 2740 (2018).
35. Vicente, J., Costa, P., Lanceros-Mendez, S., Abete, J. M. & Iturrospe, A. Electromechanical properties of PVDF-based polymers reinforced with nanocarbonaceous fillers for pressure sensing applications. *Materials (Basel)* **12**, 3545 (2019).
36. Chen, Z. et al. Three-dimensional flexible and conductive interconnected graphene networks grown by chemical vapour deposition. *Nat. Mater.* **10**, 424–428 (2011).
37. Bhagavatheswaran, E. S. et al. Construction of an interconnected nanostructured carbon black network: development of highly stretchable and robust elastomeric conductors. *J. Phys. Chem. C.* **119**, 21723–21731 (2015).
38. Haggenmueller, R., Gommans, H. H., Rinzler, A. G., Fischer, J. E. & Winey, K. I. Aligned single-wall carbon nanotubes in composites by melt processing methods. *Chem. Phys. Lett.* **330**, 219–225 (2000).
39. Chen, Y. et al. A skin-inspired stretchable, self-healing and electro-conductive hydrogel with a synergistic triple network for wearable strain sensors applied in human-motion detection. *Nanomaterials* **9**, 1737 (2019).
40. Doney, E. et al. 3D printing of preclinical X-ray computed tomographic data sets. *J. Vis. Exp.* **22**, e50250 (2013).

## Methods

**Animal tissue samples.** Sprague Dawley rats (female, 24 weeks of age, Charles River Lab) were euthanized in compliance with National Institutes of Health and institutional guidelines. Hearts were explanted immediately after euthanasia. The whole brains of young lambs (6–8 weeks of age) were obtained from the local butcher shop, within 2 h of the animal being killed. Samples were kept at room temperature and tested with a Discovery HR-2 rheometer (TA Instruments) within 12 h of tissue acquisition.

**Preparation of the alginate hydrogel substrates.** Sodium alginate with high molecular weight (FMC Biopolymer, Protanal LF 10/60) was used to prepare the ionically crosslinked alginate gels[41] and the tough IPNs[29], both as previously described. For certain studies, the polymer was irradiated with a 5 Mrad cobalt source to produce lower-molecular-weight alginate, as previously described[41]. RGD-alginate was prepared by coupling the oligopeptide GGGRGDSP (Peptides International) to the sterile alginate using carbodiimide chemistry, as previously described[12]. To form substrates for cell experiments, alginate was weighed in sterile scintillation vials and media added so that the concentration of the alginate was 2.5% (w/v). The vials were left overnight on a stir plate to allow the contents to dissolve completely. Sterilized $CaSO_4$ slurry was added to a sterile scintillation vial as well, and diluted fivefold in the corresponding medium. Crosslinked gels were fabricated as previously described[12]. The alginate–Matrigel IPN gels were fabricated as previously described[7], using reduced growth-factor, phenol-free Matrigel (Corning, 0083005).

**Preparation of agarose brain samples.** MRI data from a healthy porcine brain (permission of NeuroScience Associates of Knoxville, TN, NSALabs.com, April 2018) were used to print a plastic version of the tissue (Formlabs Form 2 3D printer, Formlabs standard resin). Ecoflex 0030 (Smooth-On, Reynolds Advanced Materials) was moulded around the plastic and left overnight to fully crosslink. Agarose powder (≥99%, Sigma-Aldrich, 9012-36-6) was mixed with water to make a 0.25% (w/v) solution, and left at 4 °C to allow the agarose to crosslink in the negative elastomeric mould. In certain studies, a drop of food colouring dye (McCormick, local grocery store) was added to the agarose solution before casting to provide contrast.

**Assessing substrate colour conformability and movement.** Yellow agarose porcine brain models were prepared as described above. Alginate gels were also prepared as per above, and dyed blue. Ecoflex 0030 films were spin-coated (Laurell Technologies, Model WS-650-23) at 400 r.p.m. (film thickness, ~100 µm). Polyimide films with a thickness of 25 µm (DuPont Kapton) were cleaned with methanol (Sigma-Aldrich) and water, and then dried. All substrate materials were laser-cut into 10 mm × 20 mm rectangles. The Ecoflex and polyimide films were coloured by painting blue hydrophobic silicone pigment (Smooth-On, Reynolds Advanced Materials) onto their surfaces. All three substrate materials were implanted at two locations on the brain models: one on an anterior portion (low radius of curvature) and the second around the posterior portion (high radius of curvature). Every sample was placed medially to laterally (starting at the midline side, gently lowering towards the lateral side). The alginate substrates were left in place for 90 s. The Ecoflex and polyimide samples were left for 5 min to allow ample time for dye transfer. The number of transferred blue pixels was quantified with ImageJ (https://imagej.nih.gov/ij/).

To explore long-term movement and conformability, substrates of alginate (300 µm) and Ecoflex 0030 (150 µm) were prepared, with the thicknesses chosen so that the bending stiffness, $D$, of each substrate, given by

$$D = \frac{Eh^3}{12(1-\nu^2)},$$

where $E$ is the elastic modulus, $h$ is the substrate thickness and $\nu$ is Poisson's ratio, was approximately the same (Supplementary Table 1).

Each substrate material was placed on a hemisphere of the brain models, on the posterior-most portion. A hydrophobic dye marked the original location of the substrate on the brain. The models were placed on Petri dishes, which were sealed with parafilm and placed on an orbital shaker (VWR Digital Shaker) at 37 °C and 100 r.p.m. to mimic brain micromotion. After 14 days, the brain models were photographed before and after the substrates were removed. The substrates were also photographed upon removal to determine whether they had flowed over the 2 weeks to conform to where they were placed.

**Cell culture studies.** Primary rat cortical astrocytes (Lonza, verified by the manufacturer to be negative for mycoplasma) were thawed and cultured in Astrocyte Growth Medium BulletKit (AGM, Lonza) following the manufacturer's guidelines. Primary rat cortical neurons (E18,19, Lonza, verified by the manufacturer to be negative for mycoplasma) were thawed before use. Neurobasal Plus Medium with 2% B27 (NBM, Lonza) was used to culture the cells, which were used directly after thawing.

The primary rat astrocytes (Lonza) in flasks were removed at passage number 6 (P6), using 0.25% trypsin–EDTA (Sigma-Aldrich), washed once in AGM, resuspended in fresh AGM and seeded on top of the preformed gels at a density of 40,000 cells cm$^{-2}$. The cells were left for 30 min in an incubator at 37 °C to begin to attach to the gels, after which further AGM was added to each well, dropwise and to the outer portion of the well to avoid disruption to the attached astrocytes. The cells were imaged every day, for 5 days, with an upright light microscope (EVOS).

The primary rat neurons (Gibco) were thawed directly before use, following the manufacturer's guidelines, without centrifugation and by suspending the cells with gentle mixing using a P1000 pipette. The neurons were seeded on top of the preformed alginate–Matrigel IPN at a density of 62,500 cells per well (~90,000 cells cm$^{-2}$). The cells were left for 15 min in an incubator at 37 °C to begin to attach to the gels, after which further NBM was gently added to each well, dropwise and to the edge of each well, so that the total volume of medium was 400 µl. Five hours after seeding the neurons, half the NBM was carefully removed and 200 µl of fresh NBM was added. The neurons were imaged every day, for 8 days, with the EVOS upright light microscope.

For the coculture experiments, ~$2 \times 10^6$ primary rat astrocytes in flasks were removed at P7, and $1 \times 10^6$ primary rat neurons were thawed. Both cell types were added to NBM medium, pipetted up and down to uniformly mix, and added on top of the gels. After 5 h of seeding, half of the NBM was carefully removed and 200 µl of fresh medium was added. The cells were imaged every day, for 5 days, with the EVOS upright light microscope.

**Immunostaining.** The astrocytes were incubated in 4% paraformaldehyde for 15 min at room temperature and washed several times using HBSS buffer supplemented with 10 mM $CaCl_2$. For antibody staining, the cells were permeabilized with 0.1% Triton X-100 in HBSS for 8 min, washed six times with HBSS with added calcium and then incubated with blocking buffer (5% goat serum and 1% bovine serum albumin). Then, the cells and gels were incubated with an antibody against GFAP (Abcam, ab33922, concentration 1:300), MAP2 (Invitrogen, PA1-10005, concentration 1:5,000), NeuN (Abcam, ab104224, concentration 1:1,000) and β3-tubulin (Abcam, ab18207, concentration 1:2,000) overnight at 4 °C. The next day, the samples were incubated with a fluorescently labelled secondary antibody (Alexa488, Abcam, concentration 1:500; goat anti-chicken Alexa 555, ab150170, concentration 1:500; goat anti-mouse Alexa 488, Invitrogen A-11029, concentration 1:500; goat anti-rabbit Alexa 555, ab150078, concentration 1:500) for 1 h at room temperature. Cell nuclei were stained with Hoechst 33342 (concentration 1:1,000) for 10 min, at which point the samples were transferred onto slides. Mounting medium (Prolong Gold Glass Antifade, Invitrogen) was added, and a coverslip placed on top of the gels. Images were taken with a Leica SP5 X MP inverted confocal microscope at ×4, ×10, ×20, ×40 and ×63 oil magnification. More than ten random fields were recorded per sample.

**Fabrication of the viscoelastic insulation materials.** PEVM was used to fabricate the insulation materials. In brief, amine-terminated PDMS ($NH_2$-PDMS-$NH_2$, aminopropyl-terminated PDMS, 100–120 cSt, Gelest), methylenebis(phenyl isocyanate) (Sigma-Aldrich, 0.4 equiv.) and isophorone diisocyanate (Sigma-Aldrich, 0.6 equiv.) were treated as previously described to synthesize PDMS–MPU–IU, a robust self-healing material[30]. PDMS–MPU–IU was dissolved in $CHCl_3$ (anhydrous, ≥99%, Sigma-Aldrich) and placed on a shaker (ThermoFisher Scientific) overnight to create a uniform viscous solution, and then $NH_2$-PDMS-$NH_2$ monomer was added to the dissolved PDMS–MPU–IU. The resulting solution was dispensed evenly over the surface of a cleaned polyethylene terephthalate (Sigma-Aldrich) film and left to crosslink for 3 h at room temperature under ambient conditions. Then, the film was placed in an oven at 65 °C to remove any traces of $CHCl_3$. The presence of exposed amine functional groups was confirmed using Fourier transform infrared spectroscopy (Bruker Hyperion 3000 FTIR Microscope), through the presence of peaks at around 3,400 cm$^{-1}$.

**Fabrication of the encapsulation materials.** To fabricate the encapsulation material, the TG and PEVM films were covalently coupled using carbodiimide chemistry. *N*-(3-Dimethylaminopropyl)-*N*′-ethylcarbodiimide hydrochloride (EDC, Sigma-Aldrich) and *N*-hydroxysulfosuccinimide (sNHS, ThermoFisher Scientific) were combined in a 1:1 ratio and a 0.1 M MES buffer (Sigma-Aldrich), adjusted to pH 6, was added to give EDC and sNHS concentrations each of 0.033 mg µl$^{-1}$. The resulting solution was dispensed onto the surface of the TG, which was then lowered onto the unmodified PEVM film and firmly pressed to remove any air bubbles and left overnight.

**Fabrication of the conductive gels.** The initial step in the fabrication of both the nanoCGs and microCGs was the same. Defect-free GFs (1.39 mg ml$^{-1}$; Supplementary Methods) and/or CNTs (Nanocyl, NC3100) were combined in 2% (w/v) alginate solution, the mixture briefly vortexed and then placed in a sonicator bath (Grainger Industrial Supplies). To form the nanoCGs, a dispensed amount of conductive gel solution was placed in a bath of 100 mM $CaCl_2$ ($CaCl_2$ dihydrate, Sigma-Aldrich) and rinsed with deionized water.

To fabricate the microCGs, the well-mixed precursor solution was dispensed onto a clean surface and rapidly moved to a freezer (−20 or −80 °C). The frozen gels were moved to a lyophilizer (Freezone, Labconco) overnight. Once removed from the lyophilization tube, the dried gels were crosslinked with 100 mM

$Ca(NO_3)_2$ (Sigma-Aldrich) in ethanol and left for at least 30 min. The gels were then rinsed with 100% ethanol and dried again.

To characterize the electrical behaviour of the gels, 5 mm × 15 mm × 300 µm conductive gels were cast in 3D printed moulds (Objet30 Pro printer, Stratasys). To fabricate gels with integrated electrical tracks in complete devices, the gels were cast in 3D printed moulds with dimensions 300 µm × 15 mm × 200 µm with a pad of 600 µm × 4 mm and electrodes with a diameter of 700 µm.

**Patterning the encapsulation layer.** A Helix 75 W laser (Epilog CO2 Laser Cutter) with a beam diameter of 127 µm was used to create openings in the encapsulation layer at the sites where the electrodes were desired. The power was adjusted from 7 to 16%, depending on the thickness of the layer and the specific type of gel, the speed was set at 30% and the frequency at 420 Hz. All files were drawn in CoralDRAW (Graphic Design Software) and printed as hairline features.

**Assembly of the complete device.** AutoCAD (Autodesk) software was used to design a positive mould of the electrical components (pads, tracks and electrode sites) with the same dimensions as the final design. The electrode sites were extruded an additional 400 µm. The pieces were printed with a clear rigid photopolymer resin (PolyJet, Stratasys) using a 3D printer (Objet30 Pro, Stratasys) and dried in an oven.

Ecoflex 0030 (Smooth-On) was mixed in a 1:1 ratio of A:B, and a small amount of blue hydrophobic dye (Smooth-On, Silicone Pigment) was added, cast over the positive moulds and left at 65 °C to crosslink for 2 h to form a flexible negative mould of the design. Next, the entire length of the tracks was filled with a uniformly suspended conductive gel formulation and a nanoCG or microCG was fabricated. The surface of the flexible mould was completely dried and then aligned with the PEVM-facing surface of the encapsulation layer, and the crosslinked tracks were transfer-printed onto the substrate. Finally, a connector with a pitch of 1 mm (designed by the Laboratory for Soft Bioelectronics Interfaces (LSBI), École Polytechnique Fédérale de Lausanne) to match the pitch of the pads was aligned with the pads, and the encapsulation housing piece was aligned from the electrode sites to the connector. The encapsulation layer covered the connector, and the assembled device was left for 24–48 h to allow the PEVM layers to self-heal together. A large 2 mm × 3 mm glass slide was left over the encapsulation piece to accelerate the self-healing process.

**Mechanical testing.** All tests were performed in ambient conditions. To measure the rheological properties of the tissues (lamb cortex and rat heart) and all synthetic materials (ionically crosslinked alginate, TG, agarose gels and conductive gel formulations), a Discovery HR-2 rheometer (TA Instruments) with a 20-mm flat plate geometry was used to test all samples with the same procedure file. The gap between the two plates was always greater than 2 mm (2,430 µm on average), and all samples tested were trimmed as needed so that they did not spill over when compressed. The synthetic gels were cast in a 12-well non-tissue culture plate with a well diameter of 20 mm. The rheometer stage was set at 37 °C and a strain sweep test (at 1 Hz) was performed on each sample, followed by a frequency sweep test (at 0.5% strain). No pre-stress was applied to any sample for any measurement. If a sample failed to completely fill the gap between the plates, it was discarded.

To evaluate the surface properties of the tissues and hydrogels, a G200 nanoindentator (Keysight Technologies) with a flat punch tip (98 µm) was used. At least five measurements per sample were taken, and no more than ten measurements, to minimize the potential effects of the sample drying. The tip was cleaned after every five measurements and after each sample was tested to remove any residues or aggregates from the previous sample.

The PEVM, Ecoflex, PEVM/TG composite and TG films were also evaluated with a tensile machine (Instron model 3342) with a 50-N load cell. All samples were laser-cut to the same gauge length of 5 mm. Thin (25 µm) polyacrylic films were placed on either side and at both ends of the rectangular samples to prevent slippage. After the films were secured, the load cell moved upwards at a rate of 1 mm $s^{-1}$ until the film fractured. The elongation (mm) and stress (MPa) were recorded. The elastic modulus of each material was extracted from the initial linear region of the resulting stress–strain graph.

**Structural characterization.** SEM images of the samples were obtained using a Hitachi SU8230 field emission scanning electron microscope. The samples were completely dried, mounted on small SEM stubs (Ted Pella) with carbon tape (Ted Pella) and then 5 nm of Pt/Pd (80:20) was deposited (EMS 300T D Dual Head Sputter Coater, Quarum/EMS) on the surfaces using a current of 40 mA.

**Porosity characterization.** Conductive gels of various compositions were cast and crosslinked, predominately by the microCG method. The gels were placed in deionized water, and then onto a dry plastic dish to remove any excess water. The mass of the gels was measured in the hydrated state. Next, the water was wicked away with a Kimwipe to remove water from the pores. The gels were weighed again, and the difference in mass divided by the final mass gave the percentage porosity of the samples.

**Resistance and conductivity characterization.** The resistance, $R$, of free-standing tracks with varying amounts of GFs and/or CNTs with dimensions of 400 µm × 15 mm and a thickness of 200 µm was measured by a four-point probe method using a Hioki RM3544 resistance meter under ambient conditions. The conductivity, $\sigma$ (S $m^{-1}$), was calculated using the following formula[42]:

$$\sigma = \frac{s}{twR}$$

where $s$ is the spacing of the pins of the four-point probe (2.54 mm), $t$ is the thickness of the gel measured (250 µm) and $w$ is the width of the gel (400 µm). To confirm the calculated $\sigma$ values, the resistance of a subset of larger samples (5 mm × 15 mm × 200 µm) was measured and the conductivity compared. A multimeter (Digilent, Digikey) was used to measure the intertrack resistance using d.c. current.

**Impedance characterization and cyclic voltammetry.** A zero-insertion-force (ZIF) connector (designed by LSBI to match the corresponding ribbon cable connector) was connected to the free end of the connector. A PalmSens4 potentiostat (PalmSens) was used to record the impedance of the exposed electrode the entire length of the electrical track (15–20 mm). The working electrode of the PalmSens potentiostat was connected to a jumper cable that was able to clip to each pin of the ZIF. A platinum counter electrode (BioLogic), with a surface area of 0.7 $cm^2$, and a Ag/AgCl reference electrode (Ohaus, 30059253) were used. The impedance behaviour was characterized for a frequency sweep from 1 MHz to 1 Hz, measuring ten points per decade. The PalmSens4 potentiostat was also used for cyclic voltammetric analysis of the electrode stability. The code used for Fig. 5c–g is available from ref. [43]. Three scans were performed at a rate of 0.1 V $s^{-1}$, typically with a range from −1 to 1 V. This voltage range was increased to −4 to 4 V when determining the water window of some of the carbon-based conductive gel formulations.

**Ageing of the arrays.** Fully assembled arrays were placed in a Petri dish that contained PBS with 2 mM $CaCl_2$ (the $Ca^{2+}$ was added to prevent the alginate gels from dissociating) and then sealed with parafilm to prevent the solution from drying out. After 84 days, the devices were removed and the impedance spectra and intertrack resistance were measured. The devices were placed such that the connector end, which plugs into the ZIF board, was not in contact with the saline solution, as this would have affected the functionality of the pins.

All animal procedures were performed in compliance with National Institutes of Health and institutional guidelines, with approval by Harvard University Institutional Animal Care and Use Committee. A mouse was terminally anaesthetized and then intubated with a MiniVent ventilator for mice (Model 845). The fur was removed and blunt dissection performed to expose the muscle underneath. Each array was placed directly on top of the rib cage, and PBS was added to keep the array hydrated. The stroke volume was set to 250 µl and the stroke rate to 150–200 strokes $min^{-1}$, and the array left for 90 min (~10,000 cycles) or 6 h (~100,000 cycles). Impedance spectra were measured after the cycling, and the impedance at 1 kHz was normalized to the impedance spectra at 1 kHz before cycling (Day 84/Day 0).

**In vivo validation.** All animal procedures were performed in compliance with National Institutes of Health and institutional guidelines with approval by Harvard University Institutional Animal Care and Use Committee or the Veterinary Office of the canton of Geneva in Switzerland. For the cardiac studies, two C57BL/6J (Jackson Laboratory) 18-week-old male mice were euthanized with $CO_2$ and then immediately placed on a warm pad with sterile gauze. A clean device was placed on the surface of the heart and connected to a compatible custom-made printed circuit board (PCB) with 32 pins. Clips were connected to the pins and to the cut ends of a sensor cable electrode pad (CAB-12970 ROHS, SparkFun). The electrode cable was connected to a soldered AD8232 Heart Rate Monitor board (SparkFun), the AD8232 Heart Monitor was connected to a computer by universal serial bus (USB) connection and a custom Matlab code was used to visualize and save each recording session. After the recordings, the files were processed using a custom Matlab code with a Savitzky–Golay filter. The raw and filtered files were saved, and each ECG was superimposed, averaged and saved. Control experiments were performed by recording from the device in air, and in contact with the exposed liver of the mouse.

The neural recordings were performed in Geneva, Switzerland in compliance with all relevant regulations under licence GE 174_17. A W-Tg (Thy1-COP4/YFP, NBRP 0685) transgenic female adult rat (~300 g body weight) was anaesthetized with a mix of ketamine (50–90 mg per kg body weight) and xylazine (5–10 mg per kg body weight) diluted in NaCl before being head-fixed into a stereotaxic frame (David Kopf Instruments). A small craniotomy was performed and the ECoG array was placed epidurally onto the cortical surface such that the eight electrodes were in intimate contact with the exposed tissue. The array had the same PCB connection set-up as described above, and the PCB was then connected to a pre-amplifier (MCS Wireless HS-32). A diode-pumped solid-state blue laser (473 nm, Laserglow Technologies) was coupled to a fibre optic connector with physical contact (FC/PC) terminal, connected to a 200 µm core optical fibre (ThorLabs) to deliver optical stimulation. The fibre was placed at the centre of

the electrode grid and positioned using a micromanipulator. A silver ground wire was fixed to the skull using a metallic screw. Optical stimulation was delivered through the transparent viscoelastic device to stimulate the cortical surface. The laser frequency was 2 Hz, with a 5 or 10 ms duration, and the intensity was varied from 35 to 90 mW. Differential recordings, triggered by the laser stimulation, were carried out with a custom code, implemented with a wireless amplifier system (Multichannel Systems Wireless W2100), at a sampling rate of 2 kHz, and a digital Butterworth bandpass filter of 1–200 Hz. The recorded signals were averaged over each individual optical pulse, across 13 recording sessions, each of ~2 min. The procedure was repeated for two viscoelastic arrays, changing the orientation of the device on the cortex as well as the location of the laser stimulation. A control experiment was performed with an agarose brain and the same set-up as described above to exclude any signal generation due to a photoelectric effect.

For the AEP measurements, a wild-type female adult rat (200 g body weight) was anaesthetized with a mix of ketamine (100 mg per kg body weight) and xylazine (10 mg per kg body weight, diluted with saline) before being head-fixed into a stereotaxic frame (David Kopf Instruments). After removing the temporal muscle, a small craniotomy was performed on the temporal lobe over the auditory cortex (anterior/posterior (A/P) = −2.7 to −5.8 mm, medial/lateral (M/L) = ±6.4 to ±8.67 mm from bregma), the dura mater was removed and a smaller (three-electrode) viscoelastic ECoG device was placed subdurally onto the cortical surface such that the electrodes were in intimate contact with the exposed tissue. The ground was a metallic screw inserted over the frontal part of the brain through the skull. Differential recordings were performed with a wireless amplifier system (Multichannel Systems Wireless W2100) at a sampling rate of 2 kHz over a frequency range of 1–90 Hz. The auditory stimulation was performed using a free-field speaker playing ~120 tone bursts at a frequency of 1 Hz (500 ms ON, 500 ms OFF) over multiple sessions varying the sound frequency (baseline, 1, 2, 5 and 10 kHz). The AEPs were averaged over all epochs per frequency to display the average and standard deviation for each experimental set. Three different sets of devices were tested sequentially.

For the muscular stimulation, C57BL/6J (Jackson Laboratory) 20-week-old female mice were anaesthetized with isoflurane and then cervically dislocated. The skin over the hindlimb was removed and the gastrocnemius exposed. An array was placed over the muscle and connected to a function generator (33210A, Keysight). A needle was inserted under the skin of the mouse. Pulses of 300 µs width and voltage intensities from 0 to 3 V were applied every 1, 2 or 5 s. The electrode that applied the stimulation was changed and/or the device was repositioned to stimulate either a single digit, the foot only, the ankle only, the entire limb (ipsilateral) only or both the ipsilateral and contralateral limbs. The stimulation was confirmed with at least three electrodes from three devices.

**Statistical analysis.** Statistical analysis was performed with GraphPad Prism9 software. One-way ANOVA and Tukey HSD post hoc tests were performed to compare different conditions. At least 5–15 random fields of view, for image comparisons, were taken and quantified.

**Reporting Summary.** Further information on research design is available in the Nature Research Reporting Summary linked to this article.

## Data availability

The data sets generated during and/or analysed during the current study are available from the corresponding author upon reasonable request. Figure 6 has associated raw data (the electrocorticography recordings), shown in Supplementary Fig. 28, and the raw files are available upon request.

## Code availability

The code associated with the work of this manuscript is available at https://doi.org/10.7910/DVN/8K77QG (ref. [43]).

## References

41. Rowley, J. A., Madlambayan, G. & Mooney, D. J. Alginate hydrogels as synthetic extracellular matrix materials. *Biomaterials* **20**, 45–53 (1999).
42. Topsoe, H. *Geometric Factors in Four Point Resistivity Measurement. Bulletin No. 472-13* (IISERKOL, 1966). http://four-point-probes.com/haldor-topsoe-geometric-factors-in-four-point-resistivity-measurement/
43. Tringides, C. & Vachicouras, N. Impedance spectra and cyclic voltammetry analysis. Harvard Dataverse, V1 (2021); https://doi.org/10.7910/DVN/8K77QG

## Acknowledgements

The authors thank T. Sirota and P. Machado, both at the Wyss Institute, Boston Massachusetts, for their help with 3D printing and the machining of moulds, respectively. This work was supported in part by the Center for Nanoscale Systems at Harvard University, which is a member of the National Nanotechnology Infrastructure Network, which is supported by the National Science Foundation under award no. 1541959. We thank the Weitz lab for the use of their rheometer, which is funded by the Materials Research Science and Engineering Center of Harvard University under National Science Foundation award no. DMR 14-20570. This work was supported by an NSF GRFP to C.M.T., as well as funding for C.M.T. through an NIH grant awarded to D.J.M. (RO1DE013033), NSF MRSEC award DMR 14-20570 and funding by the Wyss Institute for Biologically Inspired Engineering at Harvard University. I.d.L. was supported by the National Cancer Institute of the National Institutes of Health under award no. U01CA214369. The content is solely the responsibility of the authors and does not necessarily represent the official views of the National Institutes of Health. H.W. gratefully acknowledges funding support from the Wyss Technology Development Fellowship. B.R.S. is supported by the National Institute of Dental and Craniofacial Research (R01DE013349) and the Eunice Kennedy Shriver National Institute of Child Health and Human Development (P2CHD086843). A.E.-A. received funding for this work from the European Union's Horizon 2020 research and innovation programme through a Marie Sklodowska-Curie grant agreement no. 798504 (MECHANOSITY). K.K., C.C. and Y.S. were mainly funded by the EPSRC Programme Grant 2D-Health (EP/P00119X/1). C.C. acknowledges support by the EPSRC (EP/N010345/1). N.V., A.T., F.F. and S.P.L. were funded by the Bertarelli Foundation, the Wyss Center Geneva and SNSF Sinergia grant no. CRSII5_183519.

## Author contributions

C.M.T. and D.J.M. conceived the work and designed the experiments. C.M.T. characterized all the materials and developed the conductive gels, as well as fabricated and characterized all the devices. Y.S., C.C. and K.K. synthesized and provided the graphene material. C.M.T. and H.W. developed and synthesized the PEVM. C.M.T. and A.E.-A. made the material for the alginate gels for the in vitro studies. C.M.T. and I.d.L. carried out the cardiac in vivo recordings, and C.M.T., I.d.L. and B.R.S. conducted the muscular stimulation experiments. F.F. supplied the connectors, F.F. and A.T. performed the neural in vivo recordings, and A.T. analysed the electrocorticography data. C.M.T. and N.V. conducted all the data analysis. C.M.T. and D.J.M. wrote the manuscript, and C.M.T., D.J.M. and S.P.L. discussed the results. All authors contributed to the writing and editing of the manuscript.

## Competing interests

C.M.T. and D.J.M. are inventors on a patent submitted over the viscoelastic conductors and viscoelastic arrays described in this work. C.C. is an inventor on US patent 10421875B2, which covers the graphene materials used in these studies. All the remaining authors declare no competing interests.

## Additional information

**Supplementary information** The online version contains supplementary material available at https://doi.org/10.1038/s41565-021-00926-z.

**Correspondence and requests for materials** should be addressed to D.J.M.

**Peer review information** *Nature Nanotechnology* thanks Rylie Green, Bozhi Tian and the other, anonymous, reviewer(s) for their contribution to the peer review of this work.

**Reprints and permissions information** is available at www.nature.com/reprints.

nature research

Corresponding author(s): Mooney

Last updated by author(s): Apr 7, 2021

# Reporting Summary

Nature Research wishes to improve the reproducibility of the work that we publish. This form provides structure for consistency and transparency in reporting. For further information on Nature Research policies, see our Editorial Policies and the Editorial Policy Checklist.

## Statistics

For all statistical analyses, confirm that the following items are present in the figure legend, table legend, main text, or Methods section.

| n/a | Confirmed | |
|---|---|---|
| ☐ | ☒ | The exact sample size (*n*) for each experimental group/condition, given as a discrete number and unit of measurement |
| ☐ | ☒ | A statement on whether measurements were taken from distinct samples or whether the same sample was measured repeatedly |
| ☐ | ☒ | The statistical test(s) used AND whether they are one- or two-sided<br>*Only common tests should be described solely by name; describe more complex techniques in the Methods section.* |
| ☒ | ☐ | A description of all covariates tested |
| ☒ | ☐ | A description of any assumptions or corrections, such as tests of normality and adjustment for multiple comparisons |
| ☐ | ☒ | A full description of the statistical parameters including central tendency (e.g. means) or other basic estimates (e.g. regression coefficient) AND variation (e.g. standard deviation) or associated estimates of uncertainty (e.g. confidence intervals) |
| ☐ | ☒ | For null hypothesis testing, the test statistic (e.g. *F*, *t*, *r*) with confidence intervals, effect sizes, degrees of freedom and *P* value noted<br>*Give P values as exact values whenever suitable.* |
| ☒ | ☐ | For Bayesian analysis, information on the choice of priors and Markov chain Monte Carlo settings |
| ☒ | ☐ | For hierarchical and complex designs, identification of the appropriate level for tests and full reporting of outcomes |
| ☒ | ☐ | Estimates of effect sizes (e.g. Cohen's *d*, Pearson's *r*), indicating how they were calculated |

*Our web collection on statistics for biologists contains articles on many of the points above.*

## Software and code

Policy information about availability of computer code

| | |
|---|---|
| Data collection | Matlab 2019b and MCS Multi Channel Experimenter were used to collect the in vivo data. PalmSens 7 was used to collect the impedance spectroscopy of the arrays. |
| Data analysis | Matlab 2020a and GraphPad Prism 9 were used to analyse and/or plot the data. ImageJ was used to quantify the cells. Adobe Illustrator was used to make the illustrations. |

For manuscripts utilizing custom algorithms or software that are central to the research but not yet described in published literature, software must be made available to editors and reviewers. We strongly encourage code deposition in a community repository (e.g. GitHub). See the Nature Research guidelines for submitting code & software for further information.

## Data

Policy information about availability of data

All manuscripts must include a data availability statement. This statement should provide the following information, where applicable:

- Accession codes, unique identifiers, or web links for publicly available datasets
- A list of figures that have associated raw data
- A description of any restrictions on data availability

The data sets generated during and/or analysed during the current study are available from the corresponding author upon reasonable request.

# Field-specific reporting

Please select the one below that is the best fit for your research. If you are not sure, read the appropriate sections before making your selection.

☒ Life sciences ☐ Behavioural & social sciences ☐ Ecological, evolutionary & environmental sciences

For a reference copy of the document with all sections, see nature.com/documents/nr-reporting-summary-flat.pdf

# Life sciences study design

All studies must disclose on these points even when the disclosure is negative.

| | |
|---|---|
| Sample size | The study is aimed at the development and characterization of new materials in which to build surface arrays. No specific hypothesis was tested. An equal number of gels were fabricated for each condition tested, with a consistent number of cells seeded onto each gel. The in vitro data with cells (neurons, astrocytes) were done with n=4 gels, for each condition investigated. n=4 was determined to confirm uniformity of the gels manufactured and is typically used in the field. More than 10 fields of views were imaged/gel to guarantee complete characterization of the gel-cell interaction. Each experiment was repeat three times for repeatability. |
| Data exclusions | No data was excluded from the manuscript. |
| Replication | We repeated each of the cell experiments (neurons, astrocytes) three separate times (3 different batches of gels, 3 different vials of cells) and found that the results were confirmed. |
| Randomization | Cells were added onto the gels in random order (i.e. not, all MVEG soft, all MVEG stiff etc), to allow for a uniform distribution of cells amongst each condition. |
| Blinding | Blinding was not relevant to the study, as multiple fields of view were imaged from each gel condition. |

# Reporting for specific materials, systems and methods

We require information from authors about some types of materials, experimental systems and methods used in many studies. Here, indicate whether each material, system or method listed is relevant to your study. If you are not sure if a list item applies to your research, read the appropriate section before selecting a response.

## Materials & experimental systems

| n/a | Involved in the study |
|---|---|
| ☐ | ☒ Antibodies |
| ☐ | ☒ Eukaryotic cell lines |
| ☒ | ☐ Palaeontology and archaeology |
| ☐ | ☒ Animals and other organisms |
| ☒ | ☐ Human research participants |
| ☒ | ☐ Clinical data |
| ☒ | ☐ Dual use research of concern |

## Methods

| n/a | Involved in the study |
|---|---|
| ☒ | ☐ ChIP-seq |
| ☒ | ☐ Flow cytometry |
| ☒ | ☐ MRI-based neuroimaging |

## Antibodies

| | |
|---|---|
| Antibodies used | Anti-GFAP (Abcam, ab33922, [EP672Y]), concentration 1:300, Lot No: GR148838, Rabbit monoclonal<br>Anti-MAP2 (Invitrogen, PA1-10005), concentration 1:5000, Chicken polyclonal<br>Anti-NeuN (Abcam, ab104224, [1B7]), concentration 1:1000, Lot No: GR3341933, Mouse monoclonal<br>Anti-beta III tubulin (Abcam ab18207), concentration 1:2000, Lot No: Lot No: GR3259047, Rabbit polyclonal |
| Validation | Valdidation statements from vendor websites:<br>https://www.abcam.com/gfap-antibody-ep672y-ab33922.html<br>https://www.thermofisher.com/antibody/product/MAP2-Antibody-Polyclonal/PA1-10005<br>https://www.abcam.com/neun-antibody-1b7-neuronal-marker-ab104224.html<br>https://www.abcam.com/beta-iii-tubulin-antibody-neuronal-marker-ab18207.html |

## Eukaryotic cell lines

Policy information about cell lines

| | |
|---|---|
| Cell line source(s) | Rat Primary Cortical Astrocytes (Gibco), Catalog number N7745100<br>Primary rat cortex neurons, Gibco, Catalog number A1084001 |

| | |
|---|---|
| Authentication | Cell lines were authenticated by the manufacturer by which the cells were received. |
| Mycoplasma contamination | All the cell lines used in this work have been routinely tested for mycoplasma infection. |
| Commonly misidentified lines (See ICLAC register) | The cell lines used in this study are NOT present in the ICLAC register. |

## Animals and other organisms

Policy information about studies involving animals; ARRIVE guidelines recommended for reporting animal research

| | |
|---|---|
| Laboratory animals | W-Tg(Thy1-COP4/YFP) (NBRP 0685, Kyoto, Japan) transgenic female adult rat (~300 g body weight), 8 months<br>C57BL/6J male mice, from Jackson Laboratory, 18 weeks |
| Wild animals | This study did not involve wild animals. |
| Field-collected samples | This study did not involve field-collected samples. |
| Ethics oversight | Both Harvard Institutional Animal Care and Use Committee, and the Veterinary Office of the Geneva Canton of Switzerland approved the protocols used. |

Note that full information on the approval of the study protocol must also be provided in the manuscript.